Plasma Driven Exsolution for Nanoscale Functionalization of Perovskite Oxides

Vasileios Kyriakou,[a,b] Rakesh Kumar Sharma,[a] Dragos Neagu,[c] Floran Peeters,[a] Oreste De Luca,[d] Petra Rudolf,[d] Arunkumar Pandiyan,[a] Wonjong Yu,[e] Suk Won Cha,[e] Stefan Welzel,[a] Mauritius C.M. van de Sanden,[a,f] and Mihalis N. Tsampas*[a]

Abstract: Perovskite oxides with dispersed nanoparticles on their surface are considered instrumental in energy conversion and catalytic processes. Redox exsolution is an alternative method to the conventional deposition techniques for directly growing well-dispersed and anchored nanoarchitectures from the oxide support through thermochemical or electrochemical reduction. Herein, we show a new method for such nanoparticle nucleation through the exposure of the host perovskite to plasma. The applicability of this new method was demonstrated by performing catalytic tests for CO_2 hydrogenation over Ni exsolved nanoparticles prepared by either plasma or conventional H_2 reduction. Compared to the conventional thermochemical H_2 reduction, there were plasma conditions that led to the exsolution of more than ten times higher Ni amount from a lanthanum titanate perovskite, which is similar to the reported values of the electrochemical method. Unlike the electrochemical method, however, plasma does not require the integration of the material in an electrochemical cell, and is thus applicable to a wide range of microstructures and physical forms. Additionally, when N_2 plasma was employed, the nitrogen species stripped out oxygen from the perovskite lattice, generating a key chemical intermediate, such as NO, rendering this technology even more appealing.

Keywords: Plasma; exsolution; metal nanoparticles; perovskites; nanostructuring

Introduction

Transition metal oxides with the perovskite structure (ABO_3) are instrumental in several catalytic transformations and energy conversion applications due to their adjustable composition, as well as ionic and electronic exchange and transport properties.[1,2] Introducing metal nanoparticles (NPs) onto these oxides' surfaces has been proven to boost their performance.[3–5] To plant these NPs, many efforts that utilize different deposition methods have been explored in order to fabricate metal NPs- perovskite supported systems, which are not only efficient in terms of preparation but also in applicability and durability.[6] Among the examined preparation routes, infiltration[4,7,8] and atomic layer deposition[9–11] are considered very promising for enhancing the properties and in turn, the performance of the parent oxide.

In the past decade, a new method for the growth of NPs onto oxide supports has emerged. In this approach, the active metal phase in its ionic form is embedded into the host oxide crystal structure under oxidizing conditions at elevated temperatures, and subsequently, is released upon reduction. When this process is carried out in a reversible manner, i.e., the active phase can re-dissolve to the parent oxide, the process is known as solid-state recrystallization[12] or intelligent self-regeneration[13,14]. The metal NPs' nucleation can alternatively be irreversible, a case referred to as redox exsolution[15]. The latter constitutes an extensive and powerful platform in which the grown NPs are well-confined due to their partial submersion into the oxide matrix.[15–21] Contrary to the NPs grown by conventional deposition methods, the nano-architectures from exsolution are anchored and well-distributed over the host oxide, offering higher efficiency and versatility to the system[22]. The above assets have rendered exsolution an exciting platform for many important scientific areas, such as environmental catalysis,[22–26] solid oxide fuel cells[16,27–29] and electrolysers,[16,30–36] as well as chemical looping[17,37].

So far, the exsolution of metal NPs has been routinely triggered by subjecting the perovskite to a reducing agent (fuel), e.g., hydrogen, at elevated temperatures (400-900 ºC) since exsolution is dictated by the lattice reduction and defects.[13,16] Apart from hydrogen, carbon monoxide and methane are other examples of fuels, which have been utilized with interesting results related to the physicochemical properties of the exsolved particles.[18] Additionally, the reduction temperature in each case strongly depends on the reducibility of the host perovskite oxide and the doped metal precipitating from the lattice. The exsolution process can be theoretically triggered by all external conditions that drive the oxygen chemical potential (p_{O2}) low enough to sufficiently reduce the perovskite crystal. Hence, electrochemical poling[16] and vacuum[18] have been already shown to force the exsolution of metal NPs. Most notably, electrochemical poling (switching) has been demonstrated to need only few minutes in order to yield arrays of finely dispersed particles at greater population density than hydrogen.[16,30,33] This is due to the combined effect of the electron influx for reducing the B-site of the perovskite lattice when imposing high voltage and the difference in p_{O2} gradient, which can be by orders of magnitude lower compared to a gaseous fuel (p_{O2} of 10^{-35} atm at 2.0 V vs p_{O2} of 10^{-18} atm with H_2).[16,38] Despite these advantages, to electrochemically trigger exsolution, the host perovskite needs to be deposited as an electrode film, thus limiting this intriguing method to electrochemical applications.

Plasma environment, on the other hand, has unique properties that can be the external stimulus for driving the perovskite reduction. Plasma constitutes a reactive, partially ionized gas that

[a] Dutch Institute for Fundamental Energy Research (DIFFER), 5612 AJ Eindhoven, the Netherlands
[b] Engineering & Technology Institute Groningen, University of Groningen, 9747 AG Groningen, The Netherlands
[c] Department of Chemical and Process Engineering, University of Strathclyde, G1 1XL Glasgow, UK
[d] Zernike Institute for Advanced Materials, University of Groningen, 9747 AG Groningen, The Netherlands
[e] Department of Aerospace and Mechanical Engineering, Seoul National University, 151-744 Seoul, South Korea.
[f] Department of Applied Physics, Eindhoven University of Technology, 5600 MB Eindhoven, The Netherlands

*Corresponding author: m.tsampas@differ.nl, orcid.org/0000-0002-4367-4457

Supporting information for this article is given via a link at the end of the document.

includes atomic radicals, species in an electronically or vibrationally excited state, electrons and (molecular) ions as in its composition. Due to the additional internal energy imparted to atoms and molecules, otherwise inert species (e.g., dinitrogen) can become highly reactive[39–43] and therefore, plasmas have been utilized for metal oxide reduction[44,45]. Moreover, the green character of this technology (electrically driven and so it can be coupled with renewable sources) provides further motivation to be explored as an alternative pathway to introduce nanoparticles.
To explore this concept, we subjected a $La_{0.43}Ca_{0.37}Ni_{0.06}Ti_{0.94}O_{3-d}$ (LCTN) perovskite (one of the few materials that has been successfully employed in both exsolution by gaseous hydrogen[16,20] and electrochemical poling[20]), capable of Ni exsolution, in the gas discharge of inert (N_2, Ar) gases, resulting in richer growth of metallic Ni NPs and at higher populations than under conventional gaseous hydrogen treatment. Interestingly, when N_2 plasma is used, apart from the electrons, the reduced N_2 charged species also participate in stripping oxygen from the perovskite, producing NO during the process. The formation of NO as the by-product adds value to this technology since it constitutes a key intermediate for the chemical industry, currently synthesized from complex and energy intensive processes.[40] This can be considered as an alternative pathway to the reduction of metal oxides,[44,45] in which nitrogen plasma is used for the reduction step and water (and/or carbon dioxide) for the oxidation with the simultaneous production of hydrogen (and/or carbon monoxide). We further demonstrate the applicability of this concept by exploiting the superior nanoarchitectures created after plasma treatment in a critical catalytic reaction for energy transition, such as the carbon dioxide hydrogenation. Our results not only prove that plasmas can enable nanostructuring of instrumental perovskite oxides but can also generate valuable chemical intermediates along the process as byproducts, rendering the present approach even more attractive for future applications.

Results and Discussion

Realization of plasma-driven exsolution concept

To explore the plasma reduction of the perovskite, an in-house built quartz tubular reactor consisting of an inductive coil linked with a radio frequency (RF) power source was used (Figure 1). A part of the quartz tube was enclosed in a furnace of the same geometry and the LCTN oxide (crystal structure shown in Figure S1) was placed in the middle of the furnace over a porous quartz frit. In this reactor different gas reactants can be introduced, either with or without turning on the plasma source.

Initially, dinitrogen gas was fed to the reactor and the temperature increased to 650 °C with 5 °C/min. The pressure of the reactor chamber was kept at 5 mbar, whilst the total flowrate was kept constant at 100 sccm. To probe the exsolution capabilities of this material under the conventional hydrogen reduction, we introduced to the reactor 5%H_2/N_2 for 2 h. Figure 2a shows a representative scanning electron microscopy (SEM) image of the LCTN surface, unveiling that Ni exsolution of finely distributed nanoparticles occurred during the exposure. The observed population density was ~80 particles·μm_{LCNT}^{-2} with an average size of 11±1nm (Figure 2b). To rule out that the reactor's low pressure caused exsolution, an identical sample was exposed to the same conditions of flow, pressure and temperature for 10 h (5 times the H_2 reduction period), but this time without hydrogen present in the gas phase. No nanoparticles were observed during the inspection by SEM (Figure S2), confirming our hypothesis on the inertness of these operation conditions. Subsequently, a third LCTN sample was subjected to N_2 gas but this time by igniting the plasma source for 1 h (Figure S3). Figure 2c displays a representative SEM image of LCTN surface after N_2 plasma exposure, which shows that the population density was double (~170 particles·μm_{LCNT}^{-2}, average size = 18±1) to what observed with H_2, while obtained in only half the exposure time.

The structure of the nanoparticles grown under H_2 gas and N_2 plasma was examined with high resolution transmission electron microscopy (HRTEM) and the results are presented in Figures 2d and 2e, respectively. For both samples the nanostructures exhibit a spherical or ellipsoid particle shape, and are socketed on the LCNT matrix, consistent with previous reports.17 The d-spacing was calculated from the lattice fringes by applying Inverse Fast Fourier Transformation (IFFT) image processing. It is clear that exsolved nanoparticle emerged from LCNT backbone, with 0.195 and 0.194 nm lattice spacing for H_2 gas and N_2 plasma, respectively, which is a lattice constant consistent with the metallic nickel (111) planes (JCPDS 00-004-0850). The interface between the two phases suggests a strong anchorage of the exsolved nanoparticles to the matrix of the host perovskite oxide for both types of treatment as expected for exsolved particles.

The X-ray photoelectron spectroscopy (XPS) analysis did not reveal significant changes to the atomic ratio of La/Ca/Ti between the as-prepared and exposed samples (Figure S4, Table S1). However, an interesting observation is that during the reduction treatment performed in N_2 plasma some nitrogen was incorporated to the surface (3.2 at. %) in the form of oxynitride species, also corroborating to the change in N_2 gas reactivity upon plasma ignition.

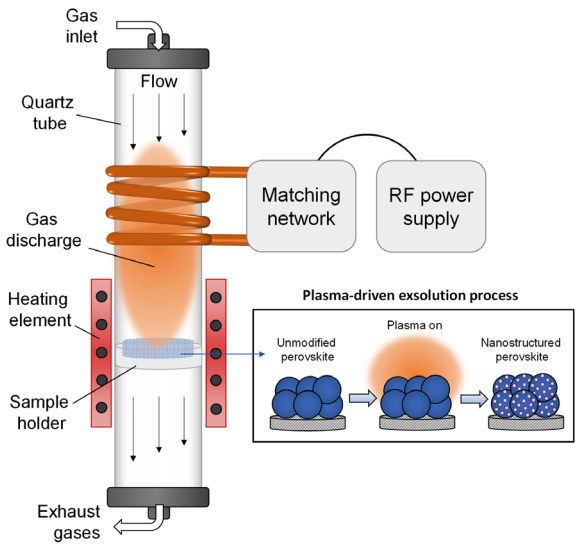

Figure 1. Schematic of the apparatus employed for realizing the plasma-triggered exsolution.

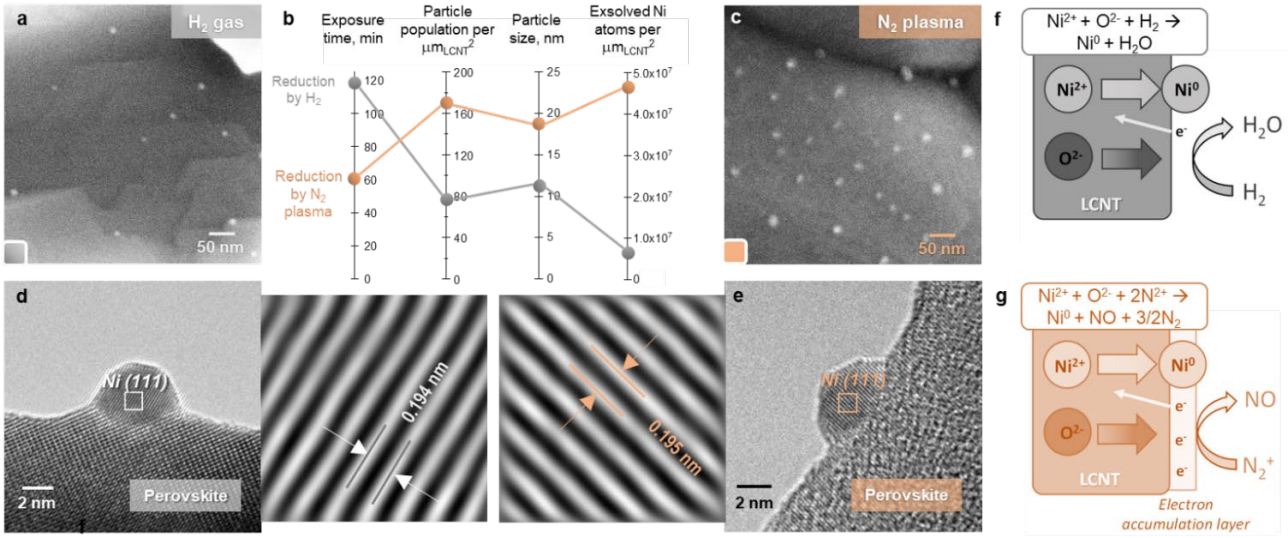

Figure 2. Characterization and possible pathways of nanoparticle exsolution. SEM and HRTEM images of the Ni nanoparticles grown on the $La_{0.43}Ca_{0.37}Ni_{0.06}Ti_{0.94}O_{3-d}$ perovskite surface after exposure to a,d. H_2 gas for 2 h (grey) c,e. N_2 plasma (orange) for 1 h at 650 °C. b. Analysis of the nanoparticle characteristics for these two cases. Pathways for Ni exsolution from LCTN during f. hydrogen gas reduction and g. nitrogen plasma exposure.

Pathways to exsolution

The quantitative analysis of the total Ni exsolved ions in Figure 2b demonstrated that N_2 plasma had a stronger effect on Ni nanoparticle nucleation than the gaseous reducing agent. As is well known from basic plasma physics,[46] since the LCTN samples treated by the plasma are electrically floating, i.e., no current can be collected by the samples, the electron and ion flux striking the LCTN surface must balance each other. Due to the difference in mobility of electrons and ions this will lead to a surface charging of the LCTN samples, repelling a part of the Maxwellian flux of the electrons and attract the ions, which in turn forms a plasma sheath. This is schematically shown in Figure 2 where the accumulated electrons on the surface of LCTN are shown. Note that this also leads to an electric field, the plasma sheath field because the plasma becomes positively charged. Of importance for the discussion of the plasma exsolution mechanism is the fact that both an electron and ion flux strike the LCTN surface where the fluxes recombine which each other, either on the surface or very close to it. This results in a stationary but dynamic electron layer on the LCTN surface, creating a negatively charged layer at the surface and thus promoting metal nucleation at more points across the surface than gas reduction, which accounts for the higher particle population observed. The flux of ions, equal to the electron flux, is given by the so-called Bohm flux (see equation S1 in SI) leading to typical fluxes of ~10^{14} species $cm_{geo}^{-2}.s^{-1}$ for N_2 plasma (see SI). It is instructive to compare this with the rate of Ni atoms exsolved, using the particle properties of Figure 2b and assuming a constant exsolution rate, which is ~10^{12} Ni atoms.$cm_{LCNT}^{-2}.s^{-1}$. This clearly shows that the Ni exsolution flux is much smaller than the ion or electron flux striking the perovskite surface. It should be noted that in one case the flux corresponds to geometrical area while in the other to perovskite area, thus a strict comparison cannot be made. Nevertheless, the effectiveness of the charged process can be approximated as ~1 in every 100 ions leads to Ni atom release.

To estimate the magnitude of the electron accumulation on the perovskite surface, we used an electrochemical sensor3 in the floating mode with respect to plasma (Figure S5). Table S2 presents the open-circuit voltage (OCV) attained by exposing one side to air and the second side to the operation conditions (plasma compartment). A strong effect of the plasma was observed since the voltage increased from 0.385 to 1.093 V with plasma ignition (Figure S6). In the absence of plasma, the OCV reflects the oxygen activity difference between the two compartments and it can be used to determine the levels of oxygen in the nitrogen compartment since the level in air compartment is known (here were calculated at 34 ppm). Under plasma exposure, the OCV increase is attributed to a net negative charge from the plasma being deposited on the plasma-facing sensor electrode since the levels of oxygen in the air compartment remain the same. The OCV values observed upon plasma conditions correspond to an equivalent oxygen partial pressure of ~10^{-25} atm (7 orders of magnitude lower than the typical 5% H_2/N_2 gas atmosphere used for exsolution[16], hence significant more reducing), providing further indication for the validity of tour hypothesis.

Our data provide evidence that electrons reaching to and residing on the perovskite surface will boost the reduction of Ni^{2+} to Ni^0. In order to compensate the charge imbalance, oxygen is driven out from the lattice to react with positively charged nitrogen species (as well as vibrationally excited or atomic nitrogen) from the plasma, further creating oxygen vacancies that may also contribute toward Ni nucleation (Figure 2g). To support this assumption, we also monitored the gaseous products released during N_2 plasma ignition by means of mass-spectrometry. The only product detected during the process was NO (Figure S7) as expected for the proposed pathway.

Opening new routes for nanocatalysts preparation

As one way of demonstrating the capabilities of this new route for developing nanostructured metal-oxide heterostructures, we compared the catalytic performance of LCTN samples treated with inert N_2, fuel H_2 and N_2 plasma in a challenging catalytic process of great interest for the energy transition, namely the CO_2 hydrogenation. Figures 3a-3c contain SEM images of the catalyst surface after the three different pretreatment conditions. As expected, no Ni particles were observed after the inert N_2 exposure for 10 h. However, upon H_2 and N_2 plasma treatment, numerous uniformly dispersed Ni nanoparticles were found at the surface of LCTN. For the catalytic testing, the samples were placed in the plasma reactor of Figure 1. The catalysts were then heated under N_2 up to 650 °C in order to carry out the different catalyst pretreatments (N_2 plasma, H_2 and inert N_2). Subsequently, the reactor pressure increased to 1 atm and the temperature decreased to 550 °C to initiate the catalytic experiments. The p_{CO2} was kept constant at 10 kPa (~10% CO_2 concentration at reactor's feed), whereas the p_{H2} was varied from 5-80 kPa (~5-80% concentration) depending on the desired p_{H2}/p_{CO2} ratio. In all cases, gaseous N_2 was employed to balance the reactor inlet. Figures 3d and 3e display the dependence of the CO_2 consumption rate on temperature and reactant ratio, respectively. The sample exposed to N_2 plasma exhibited by far the best performance, reaching up to ~140 $mmol \cdot h^{-1} \cdot gcat^{-1}$ at 550 oC with feed ratio of p_{H2}/p_{CO2} = 2. On the other hand, the maximum rate observed with the H_2 reduced sample was considerably lower and did not exceed the ~45 $mmol \cdot h^{-1} \cdot gcat^{-1}$ at the same conditions. In all cases examined, the major carbonaceous product (> 98% selectivity) was CO due to high temperatures required for activating CO_2 in the present system.

The differences shown in Figure 3 reveal a dependence of the catalytic activity on the amount of Ni exsolution. This is further confirmed by observing that the LCTN perovskite without Ni nanoparticles was practically inactive for the reaction, exhibiting detectable CO_2 reduction rate towards CO only at 550 °C. Since the activity seems to be somewhat correlated with the amount of Ni exsolution from the perovskite backbone, we tried to identify the relative surface areas of Ni nanoparticles with the N_2 plasma and H_2 samples. The analysis of Figure 3f reveal that indeed the N2 plasma exposure produced a sixfold increased Ni surface area (0.086 to 0.015 $\mu m_{Ni}^2 \cdot \mu m_{LCNT}^{-2}$) over the parent oxide compared to the conventional reduction by H2. Nevertheless, an analogous increase in the reaction rate was only observed at lower temperatures, whereas at 550 °C a threefold increase was found.

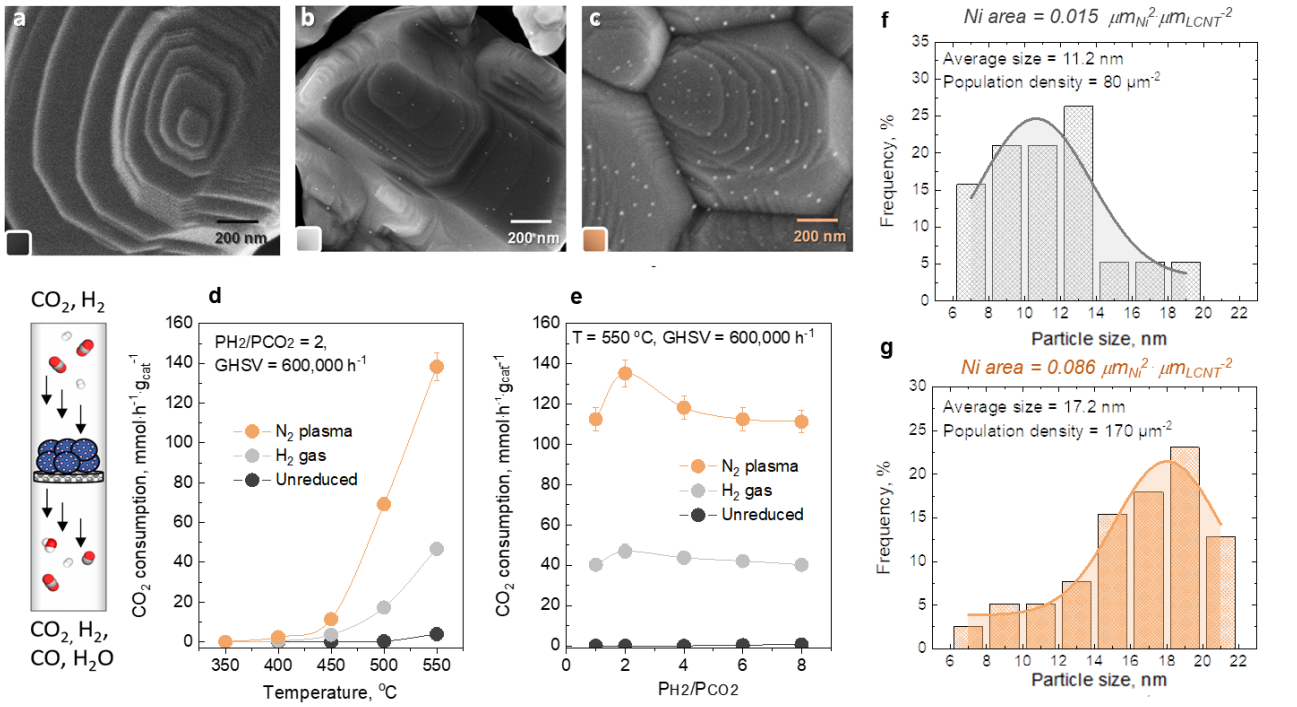

Figure 3. Exemplification of plasma exsolution in a catalysis application. SEM images of LCTN surface treatment with a. N_2 for 600 min b. H_2 for 120 min, and c. N_2 plasma for 60 min at 650 °C. Dependence of CO_2 consumption rate on d. temperature and e. reactant feed ratio for the various LCTN samples f. Exsolved nanoparticles' size and distribution following H_2 gas and N_2 plasma treatments.

Effect of plasma conditions on exsolution

To identify other factors that could affect the extent of plasma exsolution, we varied the plasma power by concurrently keeping the sample at the middle of the heating mantle, i.e., at constant distance from the coil center. In this way, the sample was located closer or farther from the plasma active zone (Figure S3). Figures 4a-c display the effect of power modification from 50-200 W on the surface morphology of the LCTN perovskite. For comparison, Figure 4b shows an SEM image of the 125 W N_2 plasma sample used in the cases described so far. By decreasing the plasma power in 50 W and thus the length of the plasma flame, the amount of the exsolved Ni nanoparticles declined to 25 from 170 particles·μm_{LCTN}^{-2}. The amounts of Ni precipitated at 50 W are slightly lower to the corresponding from H_2 exposure (Figure 2), revealing a threshold in which plasma is better than the conventional thermochemical reduction. Nonetheless, by exposing the sample closer to the plasma active zone through a power rise to 200 W, a threefold increase of Ni nanoparticles to 550 particles·μm_{LCTN}^{-2} was observed. By taking into account the particle diameter, we calculated the amount of Ni atoms exsolved in each case. As expected, the sample exposed closer to the center of the active plasma zone released the highest amount of Ni, i.e., 1.2 x 10^8 Ni atoms·μm_{LCTN}^{-2}, which is ~3 and ~30 times higher than what was obtained with 125 and 50 W, respectively (Figure 4d).

Based on the N_2 plasma afterglow model,[47,48] the density of electrons, ions and electronically excited N_2 is expected to more than double near the sample as power is increasing from 50 W to 200 W. The density of atomic N, a long-lived species in the afterglow, is slightly increased (see SI discussion on plasma properties). These observations point to charged species from the plasma playing a vital role in accelerating the rate of exsolution. Nonetheless, with atomic N being, by far, the most dominant species in the plasma afterglow, its relevance to exsolution cannot be excluded. The chemical pathway opened for the removal of oxygen species on or near the surface by the presence of atomic N (forming NO) may be a prerequisite for accelerating exsolution.

Besides the oxygen gradient, temperature rise is also known to enhance exsolution due to the higher reducibility of these perovskites. Therefore, we monitored the temperature at the sample surface during the various N_2 plasma treatments (Figure S8) while keeping the furnace temperature constant at 650 °C. Indeed, the increase in power caused the temperature at the sample to increase by ~3, 10 and 22 degrees at 50, 125 and 200 W, respectively. Since these temperature increases are rather small, they may have a minor influence on the exsolution process. The origin of the observed significant variations in exsolved Ni nanoparticles should therefore be sought in the modification of the N_2 plasma properties and the location of the active zone with power.

To probe whether other plasmas would trigger Ni nucleation, we exposed an identical LCTN sample to Ar plasma of 30 W. This power value was selected in order to create a similar active zone tail to the case of 125 W N_2 plasma used in the characterization studies (Figure S3). Figure 4d displays representative SEM images of the surface after exposing the sample for 1 h at 650 °C (sample temperature 654.6 °C, see also Figures S5-S7). The Ar plasma produced with significantly less energy an extraordinary number of ~900 Ni particles μm^{-2} with an average diameter of 8±1 nm. The Ni NP density is probably even underestimated because their size is very small for SEM detection. Ar plasma is likely to possess a ~100 times higher electron and ion density near the sample surface compared to N_2 that also leads to a ~100 times larger electron and cation flux to the sample surface (see SI). Once again, this points to the relative importance of charged species from the plasma in the exsolution process: with Ar lacking a chemical pathway for enhancing exsolution as is the case for N_2 via atomic N species, a reasonable exsolution rate can still be achieved through a large charged particle flux to the surface.

Since several plasma technologies have been developed for surface modification or functionalization,[46,49] we also explored whether one plasma that works closer to ambient pressure (rendering its applicability simpler) would also lead to exsolution. For this, we constructed a second reactor of similar geometry to Figure 1, but this time with a microwave plasma jet source operating at ~350 mbar. Again, N_2 gas discharge was employed to investigate exsolution from LCTN.

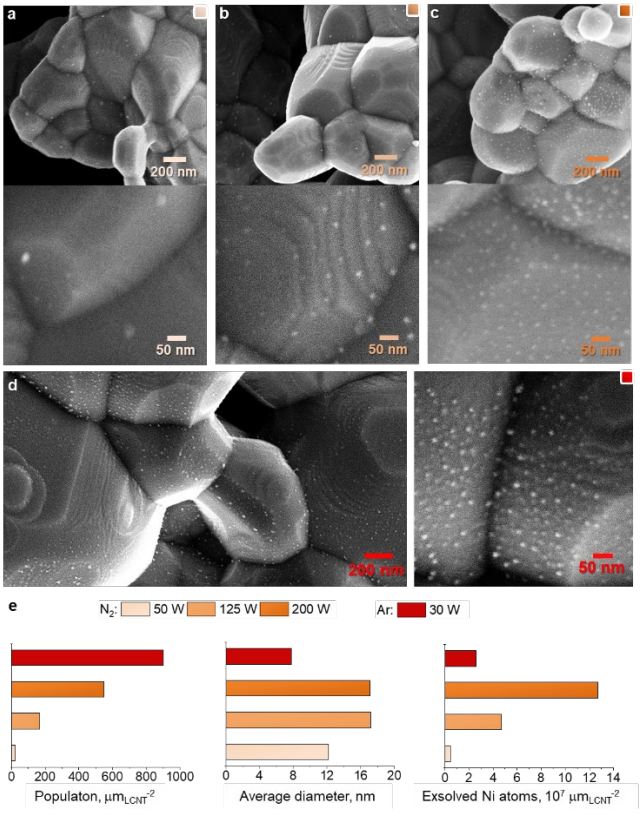

Figure 4. Effect of plasma source on exsolution. SEM images at different magnification of LCTN following treatment with a. 50 W, b. 125 W, c. 200 W powered N_2 and d. 30 W powered Ar plasma for 60 min at 650 °C. e. Population, average diameter and Ni exsolved atoms in the particles produced at different conditions of the plasma source.

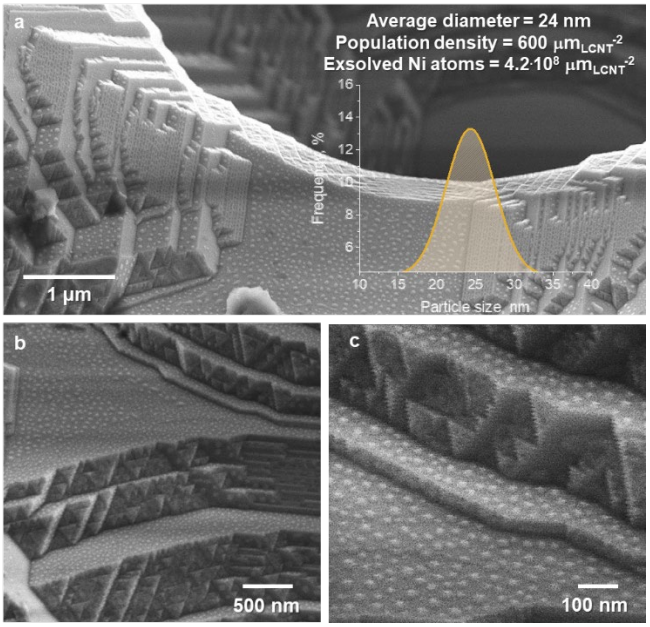

Figure 5. Demonstration of exsolution with the N_2 microwave plasma. a-c. SEM images of LCTN at different magnifications and the corresponding Ni particle analysis following the plasma treatment.

Figure 5 displays representative SEM images from LCTN surface after flowing N_2 plasma of 150 W for 1 h at 650 °C (furnace set point). Under these conditions, an impressive and dense Ni decoration of the host surface was achieved. The particle population was ~600 μm_{LCNT}^{-2} of a median diameter 24 ±1.0 nm. The amount of Ni atoms formed at the surface in this case were 4.2 x 10^8 Ni atoms·μm_{LCNT}^{-2}, which are up to ~3.5 times more than those obtained with the highest power of RF N_2 plasma. These results exemplify the flexibility of the plasma driven exsolution in terms of the utilized technology, suggesting that in future exsolution-related processes, different plasma conditions can be selected in order to fit better to the scaling up requirements.

Conclusions

We have demonstrated how plasma can be an alternative triggering agent for exsolving well-distributed and stable metal-oxide heterostructures. Similar to electrochemical switching in solid oxide cells, above certain power levels the charged species in the plasma resulted in a much faster and higher growth rate of the socketed nanoparticles than the conventional hydrogen thermochemical reduction. As opposed to the electrochemical route, however, plasmas under specific conditions are able to introduce these partly immersed and well-distributed nanostructures over high surface area functional oxides at higher rates than hydrogen thermochemical treatment, thus, enabling their use in applications beyond electrocatalysis.

Acknowledgements

This work was carried out within the SynCat@DIFFER program between the Dutch Institute for Fundamental Energy Eesearch (DIFFER), Eindhoven University of Technology (TU/e) and Syngaschem BV and funded jointly by the Netherlands Organization for Scientific Research (NWO) and Syngaschem BV. The SEM was performed within the Center for Multiscale Electron Microscopy (CMEM) with assistance from I. Schreur-Piet (TU/e). Authors thank J. van Duren (DIFFER) for assisting in the early stages of the work. Data supporting this publication are openly available under an 'Open Data Commons Open Database License - 10.5281/zenodo.5556963'. The XPS data collection was supported by the Top Research School of the Zernike Institute for Advanced Materials under the Bonus Incentive Scheme (BIS) of the Netherlands Ministry of Education, Culture and Science.

References

[2] J. Maier, *Nat. Mater.* **2005**, *4*, 805–815.
[3] P. Vernoux, L. Lizarraga, M. N. Tsampas, F. M. Sapountzi, A. De Lucas-Consuegra, J. L. Valverde, S. Souentie, C. G. Vayenas, D. Tsiplakides, S. Balomenou, E. A. Baranova, *Chem. Rev.* **2013**, *113*, 8192–8260.
[4] J. T. S. Irvine, D. Neagu, M. C. Verbraeken, C. Chatzichristodoulou, C. Graves, M. B. Mogensen, *Nat. Energy* **2016**, *1*, 1–13.
[5] L. Liu, A. Corma, *Chem. Rev.* **2018**, *118*, 4981–5079.
[6] Y. F. Sun, Y. Q. Zhang, J. Chen, J. H. Li, Y. T. Zhu, Y. M. Zeng, B. S. Amirkhiz, J. Li, B. Hua, J. L. Luo, *Nano Lett.* **2016**, *16*, 5303–5309.
[7] C. Ruocco, V. Palma, A. Ricca, *Chem. Eng. J.* **2019**, *377*, 119778.
[8] C. Yang, J. Li, Y. Lin, J. Liu, F. Chen, M. Liu, *Nano Energy* **2015**, *11*, 704–710.
[9] Y. Hajar, V. Di Palma, V. Kyriakou, M. A. Verheijen, E. A. Baranova, P. Vernoux, W. M. M. Kessels, M. Creatore, M. C. M. van de Sanden, M. Tsampas, *Electrochem. commun.* **2017**, *84*, DOI 10.1016/j.elecom.2017.09.023.
[10] H. J. Choi, K. Bae, S. Grieshammer, G. D. Han, S. W. Park, J. W. Kim, D. Y. Jang, J. Koo, J.-W. Son, M. Martin, J. H. Shim, *Adv. Energy Mater.* **2018**, *8*, 1802506.
[11] A. Pandiyan, V. Di Palma, V. Kyriakou, W. M. M. Kessels, M. Creatore, M. C. M. Van De Sanden, M. N. Tsampas, *ACS Sustain. Chem. Eng.* **2020**, *8*, 12646–12654.
[12] K. Takehira, *Catal. Surv. from Asia* **2002**, *6*, 19–32.
[13] Y. Nishihata, J. Mizuki, T. Akao, H. Tanaka, M. Uenishi, M. Kimura, T. Okamoto, N. Hamada, *Nature* **2002**, *418*, 164–167.
[14] H. Tanaka, M. Taniguchi, M. Uenishi, N. Kajita, I. Tan, Y. Nishihata, J. Mizuki, K. Narita, M. Kimura, K. Kaneko, *Angew. Chemie Int. Ed.* **2006**, *45*, 5998–6002.
[15] D. Neagu, G. Tsekouras, D. N. Miller, H. Ménard, J. T. S. Irvine, *Nat. Chem.* **2013**, *5*, 916–923.
[16] J. H. Myung, D. Neagu, D. N. Miller, J. T. S. Irvine, *Nature* **2016**, *537*, 528–531.
[17] K. Kousi, D. Neagu, L. Bekris, E. I. Papaioannou, I. S. Metcalfe, *Angew. Chemie - Int. Ed.* **2020**, *59*, 2510–2519.
[18] D. Neagu, V. Kyriakou, I. L. Roiban, M. Aouine, C. Tang, A. Caravaca, K. Kousi, I. Schreur-Piet, I. S. Metcalfe, P. Vernoux, M. C. M. Van De Sanden, M. N. Tsampas, *ACS Nano* **2019**, *13*, 12996–13005.
[19] Y. Gao, D. Chen, M. Saccoccio, Z. Lu, F. Ciucci, *Nano Energy* **2016**, *27*, 499–508.
[20] Y.-R. Jo, B. Koo, M.-J. Seo, J. K. Kim, S. Lee, K. Kim, J. W. Han, W. Jung, B.-J. Kim, *J. Am. Chem. Soc.* **2019**, *141*, 6690–6697.
[21] K. J. Kim, H. Han, T. Defferriere, D. Yoon, S. Na, S. J. Kim, A. M. Dayaghi, J. Son, T.-S. Oh, H. M. Jang, G. M. Choi, *J. Am. Chem. Soc.* **2019**, *141*, 7509–7517.
[22] D. Neagu, E. I. Papaioannou, W. K. W. Ramli, D. N. Miller, B. J. Murdoch, H. Ménard, A. Umar, A. J. Barlow, P. J. Cumpson, J. T. S. Irvine, I. S. Metcalfe, *Nat. Commun.* **2017**, *8*, DOI 10.1038/s41467-017-01880-y.
[23] G. Dimitrakopoulos, A. F. Ghoniem, B. Yildiz, *Sustain. Energy Fuels* **2019**, *3*, 2347–2355.
[24] B. Yan, Q. Wu, J. Cen, J. Timoshenko, A. I. Frenkel, D. Su, X. Chen, J. B. Parise, E. Stach, A. Orlov, J. G. Chen, *Appl. Catal. B Environ.* **2018**, *237*, 1003–1011.
[25] Y.-F. Sun, Y.-L. Yang, J. Chen, M. Li, Y.-Q. Zhang, J.-H. Li, B. Hua, J.-L. Luo, *Chem. Commun.* **2018**, *54*, 1505–1508.
[26] M. Kothari, Y. Jeon, D. N. Miller, A. E. Pascui, J. Kilmartin, D. Wails, S. Ramos, A. Chadwick, J. T. S. Irvine, *Nat. Chem.* **2021**, DOI 10.1038/s41557-021-00696-0.
[27] K. Y. Lai, A. Manthiram, *Chem. Mater.* **2018**, *30*, 2515–2525.
[28] T. Zhu, H. E. Troiani, L. V. Mogni, M. Han, S. A. Barnett, *Joule* **2018**, *2*, 478–496.
[29] T. Zhu, H. Troiani, L. V. Mogni, M. Santaya, M. Han, S. A. Barnett, *J.*

Power Sources **2019**, *439*, 227077.
[30] V. Kyriakou, D. Neagu, E. I. Papaioannou, I. S. Metcalfe, M. C. M. van de Sanden, M. N. Tsampas, *Appl. Catal. B Environ.* **2019**, *258*, 117950.
[31] V. Kyriakou, D. Neagu, G. Zafeiropoulos, R. K. Sharma, C. Tang, K. Kousi, I. S. Metcalfe, M. C. M. Van De Sanden, M. N. Tsampas, *ACS Catal.* **2020**, *10*, 1278–1288.
[32] J. G. Lee, J. H. Myung, A. B. Naden, O. S. Jeon, Y. G. Shul, J. T. S. Irvine, *Adv. Energy Mater.* **2020**, *10*, 1–6.
[33] G. Tsekouras, D. Neagu, J. T. S. Irvine, *Energy Environ. Sci.* **2013**, *6*, 256–266.
[34] L. Ye, M. Zhang, P. Huang, G. Guo, M. Hong, C. Li, J. T. S. Irvine, K. Xie, *Nat. Commun.* **2017**, *8*, 1–10.
[35] H. Lv, T. Liu, X. Zhang, Y. Song, H. Matsumoto, N. Ta, C. Zeng, G. Wang, X. Bao, *Angew. Chemie Int. Ed.* **2020**, *59*, 15968–15973.
[36] H. Li, T. Liu, P. Wei, L. Lin, D. Gao, G. Wang, X. Bao, *Angew. Chemie Int. Ed.* **2021**, *60*, 14329–14333.
[37] D. Hosseini, F. Donat, P. M. Abdala, S. M. Kim, A. M. Kierzkowska, C. R. Müller, *ACS Appl. Mater. Interfaces* **2019**, *11*, 18276–18284.
[38] Q. Lu, B. Yildiz, *Nano Lett.* **2016**, *16*, 1186–1193.
[39] C. Sun, J. A. Alonso, J. Bian, *Adv. Energy Mater.* **2020**, *2000459*, 1–21.
[40] H. Patel, R. K. Sharma, V. Kyriakou, A. Pandiyan, S. Welzel, M. C. M. van de Sanden, M. N. Tsampas, *ACS Energy Lett.* **2019**, *4*, 2091–2095.
[41] A.A. Fridman, *Plasma Chemistry*, Cambridge University Press, **2008**.
[42] R. K. Sharma, H. Patel, U. Mushtaq, V. Kyriakou, G. Zafeiropoulos, F. Peeters, S. Welzel, M. C. M. van de Sanden, M. N. Tsampas, *ACS Energy Lett.* **2020**, 313–319.
[43] A. Bogaerts, E. C. Neyts, *ACS Energy Lett.* **2018**, *3*, 1013–1027.
[44] K. S. Go, S. R. Son, S. D. Kim, *Int. J. Hydrogen Energy* **2008**, *33*, 5986–5995.
[45] K. C. Sabat, P. Rajput, R. K. Paramguru, B. Bhoi, B. K. Mishra, *Plasma Chem. Plasma Process.* **2014**, *34*, 1–23.
[46] A. J. L. Michael A. Lieberman, *Principles of Plasma Discharges and Materials Processing*, John Wiley & Sons, Inc., **2005**.
[47] V. Guerra, P. A. Sá, J. Loureiro, *Plasma Sources Sci. Technol.* **2003**, *12*, DOI 10.1088/0963-0252/12/4/314.
[48] V. Guerra, P. A. Sá, J. Loureiro, *EPJ Appl. Phys.* **2004**, *28*, 125–152.
[49] R. Snoeckx, A. Bogaerts, *Chem. Soc. Rev.* **2017**, *46*, 5805–5863.